Title

Sorafenib inhibits invasion of multicellular organoids that mimic Lymphangioleiomyomatosis nodules.

Author List

Sinem Koc-Gunel[1,2,3], Lalit K. Gautam[4], Ben A. Calvert[1,2,4], Shubha Murthy[4], Noa C. Harriott[1,2,4], Janna C. Nawroth[1,2,5,6], Beiyun Zhou[1], Vera P. Krymskaya[7], and Amy L. Ryan[1,2,4*]

Author Affiliations

[1]Hastings Center for Pulmonary Research, Division of Pulmonary, Critical Care and Sleep Medicine, Department of Medicine, University of Southern California, Los Angeles, CA, USA

[2]Department of Stem Cell Biology and Regenerative Medicine, University of Southern California, Los Angeles, CA, USA

[3]Institute of Medical Virology, University Hospital Frankfurt, Goethe University, Frankfurt, D-60596, Germany

[4]Department of Anatomy and Cell Biology, Carver College of Medicine, University of Iowa, Iowa City, IA, USA

[5]Helmholtz Pioneer Campus and Institute of Biological and Medical Imaging, Helmholtz Zentrum München, Neuherberg, Germany

[6]Biological Imaging, Central Institute for Translational Cancer Research (TranslaTUM), School of Medicine, Technical University of Munich, Munich, D-81675, Germany

[7]Division of Pulmonary and Critical Care Medicine, Lung Biology Institute, Perelman School of Medicine, University of Pennsylvania, Philadelphia, PA, USA

Contact Information

*Lead contact and Corresponding Author

Amy L Ryan, PhD

Associate Professor: Anatomy and Cell Biology

Associate Director: Center for Gene Therapy

BSB, 1-400 Core

University of Iowa

51 Newton Road

Iowa City, Iowa, 52242

E: mail: amy-l-ryan@uiowa.edu

Tel: +1 319 335 8908

Twitter: @ryanlabuiowa

Running title: Sorafenib inhibits LAM cell invasion

Abstract:

Lymphangioleiomyomatosis (LAM) is a debilitating, progressive lung disease with few therapeutic options, largely due to a paucity of mechanistic knowledge of disease pathogenesis. Lymphatic endothelial cells (LECs) are known to envelope and invade clusters of LAM-cells, comprising of smooth muscle α-actin and/or HMB-45 positive "smooth muscle-like cells" however the role of LECs in LAM pathogenesis is still unknown. To address this critical knowledge gap, we investigated wether LECs interact with LAM-cells to augment their metastatic behaviour of LAM-cells. We performed *in situ* spatialomics and identified a core of transcriptomically related cells within the LAM nodules. Pathway analysis highlights wound and pulmonary healing, VEGF signaling, extracellular matrix/actin cytoskeletal regulating and the HOTAIR regulatory pathway enriched in the LAM Core cells. We developed an organoid co-culture model combining primary LAM-cells with LECs and applied this to evaluate invasion, migration, and the impact of Sorafenib, a multi-kinase inhibitor. LAM-LEC organoids had significantly higher extracellular matrix invasion, decreased solidity and a greater perimeter, reflecting increased invasion compared to non-LAM control smooth muscle cells. Sorafenib significantly inhibited this invasion in both LAM spheroids and LAM-LEC organoids compared to their respective controls. We identified TGFβ1ı1, a molecular adapter coordinating protein-protein interactions at the focal adhesion complex and known to regulate VEGF, TGFβ and Wnt signalling, as a Sorafenib-regulated kinase in LAM-cells. In conclusion we have developed a novel 3D co-culture LAM model and have demonstrated the effectiveness of Sorafenib to inhibit LAM-cell invasion, identifying new avenues for therapeutic intervention.

Abstract word count: 243

Keywords: TGFβ1ı1, Kinases, LAM nodules, Lymphatic endothelium, Metastasis, Sorafenib.

Introduction:

Lymphangioleiomyomatosis (LAM) is characterized by the formation of neoplastic lesions comprising of tumorous smooth muscle-like (LAM-cells) and epithelioid-like cells, leading to cystic destruction of the lung interstitium, invasion of bronchioles, blood, and lymphatic vessels, resulting in severe obstructive lung disease (1, 2). To date there are limited therapeutic options for LAM patients, and it remains a severely debilitating and progressive disease disease affecting predominantly women of childbaring age. Investigating rare lung diseases is challenging because if a lack of available disease-relevant and patient-specific tissues available and animal model systems that poorly reflect the LAM-phenotype in humans (3). The cellular and molecular mechanisms that drive extensive cystic tissue remodelling of the pulmonary parenchyma are largely unknown and therefore, there is a paucity of known molecular targets for therapeutic intervention. Most cellular models study cells in isolation in a 2-dimensional (2D) culture microenvironment; they are highly reductionist models which generally loose relevant properties like differentiation, polarization, cell-cell communication, and extracellular matrix (ECM) contacts. At the same time wound healing, inflammatory processes, and hyperproliferation are artificially promoted (4). These models lack vital information on the intercellular interactions driving LAM pathogenesis.

LAM can manifest sporadically or present as part of tuberous sclerosis, driven by somatic or germline mutations in the tuberous sclerosis complex (TSC1 or TSC2) genes (5–11). LAM lesions consist of aggregations of epithelioid cells expressing HMB-45, with LAM-cells being located centrally in the nodule and expressing smooth muscle α actin (SMA) (1, 3, 12–15). The lesions in LAM were recently shown to be invaded by lymphatic endothelial cells (LECs) (16–22), however the impact of the lymphatic endothelium on the progression of the disease is poorly understood. Importantly, the recurrence of LAM lesions in transplanted lungs suggests that lymphatic involvement may influence metastasis in the lung (23).

Currently rapamycin, an mTOR Inhibitor, is the gold standard of therapy for LAM patients with declining lung function tests (24). Rapamycin allosterically inhibits activity of mTORC1, known as mammalian target of rapamycin complex 1 or mechanistic target of rapamycin complex, thereby preventing the increased cell growth, proliferation and cell survival, which occurs in LAM due to the somatic mutations in TSC2 (5, 25–29). Current LAM guidelines recommend rapamycin therapy for patients with an FEV1 <70% (24). For LAM patients with a normal lung function test, no preventive therapeutic option exists. Since LAM is a slow growing perivascular tumor, perivascular epithelioid cell neoplasm (PeCOMA), and is suspected to metastasize to other organs, multiple pathways are discussed to be involved in promoting cell detachment and trafficking of LAM-cells through the lymphatic system to other organs in current literature (18, 27, 30–32). LAM shares disease mechanisms with tumorous diseases through cytokine secretion and activation of pathways promoting cell growth (33–36). Sorafenib, an FDA-approved multi-kinase inhibitor, inhibits multiple pathways in the tumor microenvironment and has been shown to improve patient outcomes by decreasing tumor cell growth, tumor-associated-angiogenesis, and metastasis (37–39). Sorafenib also has potential therapeutic benefits by inhibiting eIF4E, eukaryotic translation initiation factor, which is upregulated in LAM downstream of mTOR activation and blocking VEGFR-2 and VEGFR-3 to prevent LAM-associated lymphangiogenesis (3, 39–41).

To address the critical need to identify new therapeutic targets for the care and treatment of patients with LAM, we developed a 3D multicellular organoid model comprising of LAM-cells and LECs to better understand the impact of cell-cell interactions in LAM progression. We then used this model system to evaluate the impact of multi-kinase inhibition, by Sorafenib, on the invasion of our LAM-spheroids and LAM-LEC organoids into the surrounding extracellular matrix.

Results:

To recapitulate the 3D structure of a LAM nodule we first evaluated LEC distribution and LAM nodule association in LAM patient lung tissues (**Fig. 1**). Using formalin-fixed, paraffin embedded (FFPE) LAM lung tissues, we evaluated the expression of SMA, indicative of LAM-cells, within LAM nodules, HMB-45, a melanocytic marker expressed on LAM-cells, vascular endothelial growth factor receptor 3 (VEGFR3) and podoplanin (PDPN) expressed on lymphatic endothelium. Cyst formation with cysts of various sizes, typical for LAM, is observed in the Hematoxilyn and Eosin (H&E) image in **Figure 1A,** highlighted by the red arrows. In the LAM tissues, LECs were clearly observed in and around, HMB-45 (PMEL)/SMA-positive LAM nodules close to cysts, highlighted by the yellow arrows. Close association of VEGFR3 and PDPN is indicative of LECs located around and within the nodules (**Fig. 1B**). LAM nodule formation can be observed in immediate proximity of cysts (white arrows), highlighting LAM-cell aggregations consisting of epithelioid-like HMB-45 positive LAM-cells as well as myofibroblast-like spindle-shaped LAM-cells as demonstrated in **Figure 1C**. This aligns with typical findings in LAM and is well-described in literature(2, 13, 21, 42, 43). LAM lung lesions are also described to be near LECs (20–22). **Figure 1C** and **1D** shows LECs invading and surrounding LAM nodules, creating channels throughout the lesion.

To further evaluate the spatial organization of LAM-cells we performed *in situ* spatial transcriptomics on two independent regions of FFPE-prepared LAM donor lung tissue (**Fig. 2-3 and Supplementary Fig. S1-2**). Transcriptomics from 3343 and 2595 spots were obtained at a median depth of 8283 and 7536 UMIs/spot and 4317 and 4090 genes/spot for LAM1 and LAM2, respectively (**Supplementary Fig. S1**). Unbiased clustering and spot features classified the spots into 7 clusters for LAM1 (**Fig. 2A-B and Supplemental Database S1).** For LAM-2 7 clusters were also identified (**Supplementary Fig. S2A-B and Supplemental Database S2**). The heat map in **Figure 2C** identifies LAM-core enriched genes (purple column) compared to the other six clusters

of genes. Expression of well established LAM identifying genes including ACTA2, VEGFD and ESR1 were significantly higher in the LAM-core (**Fig. 2C-D and Supplementary Fig. 2C-D**). Additional significant differentially expressed genes (DEGs) characteristic of the LAM-core included TGFRB3, HOXA11, HOXD11, TWIST2, UNC5D, SFRP4, RAMP1, PTGER3, NCAM1 and VEGFR3 (**data not shown).** Using LungGENS we mapped the >1.5 fold differentially expressed genes (DEG) in the LAM-CORE cluster to genes identified to be selectively expressed in lung cell types. The LAM-CORE contained mesenchymal genes (42.6%), endothelial genes (4.9%), epithelial genes (34.4%) and immune cell genes (18%), as shown in **Figure 2E**.

To determine the pathways represented by the gene expression in the LAM-core we performed Gene Ontogeny (GO) analysis on genes from each cluster with >1.5 fold up or down regulation compared to features from rest of clusters **(Fig. 2F**). The pathways most highly represented by the dataset included pathways related to the extracellular matrix including integrin and paxillin signalling, signaling pathways known to be dysregulated in LAM including VEGF and Estrogen signaling and other pathways of interest including HOTAIR regulatory pathways and kinase pathways including JAK2, STAT3 and activin inhibition signalling. The predicted relationships of signaling in the VEGF signalling pathway is shown in **Figure 2G**, highlighting predicted activation of pathways regulating cell migration, survival, lymphangiogenesis, cell-cell interactions, epithelial to mesenchymal transition and metastasis, all common features of LAM. As multiple pathways regulating kinases were confirmed to be upregulated in the LAM-core we subsequently evaluated the expression of a panel of kinases in isolated LAM-cells through a kinase array (**Fig. 2H and Supplementary Database S3**). The data shown in **Figure 2H** highlights the kinases that had a greater than a 1.25 fold change increase compared to the median protein level of all kinases. The two proteins with the highest fold change were HIPK2 and TYRO3. The heatmap in **Figure 2I** compares the relative expression of the kinases included in the kinase assay side-by-side with the gene expression from the spatialomics shown by cluster. The

genes/proteins highlighted in green are clustered together and associated with higher expression in both the kinase assay and genes in the LAM-core (**Fig. 2H-I**) and included PDGFRB, TGFB1ı1 and FGFR1.

To assign lung cell types to the spatial-transcriptomics we mapped our data to a comprehensive expression atlas of the human lung (44). The cell clusters in the spatialomics data sets mapped to 13 different lung cell types in the Lung Map Atlas as shown in **Figure 3A**. These included sub populations of mesenchymal, endothelial, epithelial and immune cells (**Fig. 3A**). LAM-core genes identified in Figure 2 and published studies (45) were most highly expressed in cells clustering in airway smooth muscle cells (ASMC), alveolar firboblasts (AF2) and the highest levels associated with cell culsters identifying as predominantly transient secondary crest myofibroblasts (SCMF) (**Fig. 3B**). SCMF are typically only present in early postnatal lung development and closely associated with AT1 cells. Infact loss of sonic hedgehog signalling from AT1 cells was recently shown to reduce SCMF and led to alveolar simplification, supporting the role of these cells in LAM disease (46). Mapping the spatial localization of the SCMF/and AF2 cells labelled LAM-core we can see that this closely associated with the lung pathology for LAM shown in Figure 2A and that the LAM-core cells are located in close association with AT2/AT1 cells (**Fig. 3C**).

Next we established methodology to reproducibly generate organoids mimicking the structure and organization of a LAM nodule, starting with the generation of spheroids of LAM-cells (**Figure 4**). We optimized cell number and media composition to reproducibly generate spheroids from either primary bronchial SMCs, as a control, or human patient-derived LAM-cells (**Fig. 4A-B**). After 24h the spheroids were embedded in Matrigel and their growth and invasion into the surrounding matrix were documented through imaging and analysis of the properties of the spheroids over a 5-day period (**Fig. 4C-D**). Invasion was measured using an image analysis command pipeline generated in CellProfiler (Broad Institute, detailed in the **Supplemental**

Information). Each mapped spheroid was checked manually, and manual spheroid edge identification was used where inaccuracies were observed due to low contrast differences between cells and background (**Supplemental Figure S3**). Application of an automated image pipeline allowed for analysis of the spheroid invasion and using this approach, we were able to compare several physical properties of the spheroids including compactness, perimeter, and solidarity. LAM spheroids has significantly greater perimeter after both 3 and 5 days of 3D culture indicating increased projections invading into the matrix **(Fig. 4E)**. This is also highlighted in the confocal images of the spheroids shown after 3 days (**Fig. 4F-G**) and 5 Days (**Fig. 4G**). After 5 days we observed PDGFRα localization in the cells invading the matrix suggesting that PDGFR signalling may be involved in the mechansism leading to increased invasion by LAM-cells (**Fig. 4G**).

To add tissue level complexity and to closely mimic a LAM nodule we integrated LECs into the LAM spheroids to create a 3D multicellular organoid model, to better evaluate cell-cell interactions in LAM pathogenesis (**Figure 5)**. Commercially available lung microvascular lymphatic endothelial cells (HpMVLEC, referred herein as LECs) were evaluated for the expression of LEC markers including expression of PDPN, PROX1 PECAM and VE-Cadherin (CD144) (**Supplemental Figure S4A-B**). PDPN expressing lymphatic endothelial cells comprised of 96.5% of the endothelial cells by FACS and IF staining (**Supplemental Figure S4B**). SMC-spheroids or LAM-spheroids were established as shown in **Figure 4**. One day prior to embedding in ECM, SMCs and LAM-cells were labelled with CellTracker™-CMFDA (green) and LEC, labelled with CellTracker™-CMTPX (red) (**Figure 5A-B**). After 24 hours co-culture, the organoid comprises of a green-labelled LAM-cells core surrounded by red-labelled LECs. The cellular distribution was confirmed through staining for SMA (green) for the LAM-cells and PDPN for the LECs (**Fig. 5C**). The organoids were embedded in ECM and monitored over 5 days (**Fig. 5D**). LAM-nodule organoids had significantly higher matrix invasion, decreased solidity, increased

compactness and a greater perimeter, reflecting increased invasion compared to SMC organoid controls (N=9; p<0.0001) (**Fig. 5E**). Evaluation of live cell images indicate that the majority of the invasion is from the green labelled LAM-cells (**Fig. 5F-G**).

LAM-cells are known to activate PI3K/AKT and ERK/MAP kinase signalling (47), in addition to possible induction of angiogenesis through VEGFR2, VEGFR3 and PDGF-mediated signalling (43, 48–50). Considering all the augmented pathways in LAM, we selected an FDA-approved multikinase-inhibitor, Sorafenib, to target several of these pathways. Sorafenib is known to inhibit VEGFR2-, VEGFR3-, PDGFRβ-mediated signaling and the phosphorylation of eIF4E and MEK1/2 and ERK1/2 (38–40). To evaluate the effect of Sorafenib, cellTracker-labelled LAM spheroids and co-cultured LAM organoids were treated with Sorafenib over 72 hours, and the impact on the invasive behaviours of the spheroids and organoids was monitored through daily imaging. Image analysis revealed a complete cessation of invasion in LAM spheroids at 7µM Sorafenib, as shown in **Figure 6A-C.** On the other hand, although the co-cultured LAM/LEC organoids continued to display invasive behavior, there was still a significant reduction in invasion overall **(Fig. 6D-F).** It is already established that LAM-cells are characterized by upregulated mTOR activity (3, 51, 52) and Rapamycin, an mTOR inhibitor, is the current and only approved therapeutic to slow the progression of LAM (24). Using our model, we compared treatment with 20 µg Rapamycin to 7 µM Sorafenib and vehicle control on invasion (**Fig. 6G-I**) and we found that while Rapamycin significantly suppressed the organoid perimeter (**Fig. 6G**) and ECM invasion (Form factor, **Fig. 6H**) it was not as efficient as Sorafenib which almost completely blocked invasion (**Fig. 6G-I and Supplemental Figure S5**).

To start to delineate the mechanism behind the complete suppression of invasion of LAM-spheroids we performed a phosphokinase array comparing vehicle to 7µM Sorafenib. The relative expression data of the proteins with greater than 30% increase or decreased expression compared to vehicle are shown in **Fig. 7A**. A significant fold change was considered, when the

value is less then 0.5 or greater than 2.0, indicating that the protein amount either decreased by 50% (0.5) or doubled (2.0). The kinase assay combined experimental replicates from one biological donor for each of vehicle and treated. A significant decrease in expression was observed for CAMK2D and EPB41L1, with EPM2A and EPHB3 were significantly increased (**Fig. 7A**). One notable protein down regulated was TGFB1ı1 (transforming growth factor beta 1-induced transcript 1), also shown in our data to be a significantly expressed protein in the kinase array (**Fig. 2H**) and associated with the LAM-core cluster in the spatial transcriptomics (**Fig. 2I**). TGFB1I1 has been implicated to have roles in the regulation of cell migration, proliferation and tissue remodelling, all critical processes in the pathogenesis of LAM, including the maintaining a contractile cellular phenotype as well as functioning as a transcriptional cofactor to modulate gene expression. TGFB1I1 is a TGFβ-regulated gene that shares extensive homology with paxillin, with roles as a focal adhesion protein interating with ECM components such as collagen 1. Sorafenib-mediated inhibition of TGFB1I1 reduced the growth and migration of LAM-cells suggesting that TGFB1I1 may contribute to this process through the regulation of the downstream effects of TGFβ1 signaling. STRING analysis also highlights significant interactions of TGFB1ı1 with proteins involved in β-catenin binding and VEGF signalling (**Fig. 7B**), proteins in these networks also correlate with higher gene expression in the LAM-core clusters in the spatialomics datasets **(Fig. 7C).** Overall this suggests that TGFB1ı1 may be a Sorafenib-sensitive core regulator in the pathogenesis of LAM which warrants further investigantion to delineate the precise mechansims.

Discussion:

In this study we have created a human multicellular organoid model in which the role of LECs in the progression of LAM can be evaluated. By creating 3D unicellular spheroids and multicellular organoids, including LECs, we generated a model that moves closer to reflecting the composition

of a LAM nodule where we (**Fig. 1**), and others, have shown that LECs invade clusters of LAM-cells in donor lung tissues (18, 53, 54). We demonstrate significant changes in the invasive and metastatic behavior comparing LAM-cells to primary bronchial SMCs where SMCs disperse and organize in the ECM, while LAM-cells have an expanding spherical core with cells expressing high levels of PDGFRα invading the matrix, suggesting that PDGFRα may be important in the invasive/metastatic spread of LAM (55–57).

LAM patients with reduced lung function respond to Rapamycin resulting in stabilization of lung function (58–62). However, Rapamycin is also known to be primarily cytostatic and not cytotoxic, limiting the inhibition of tumorous growth and is currently only available for patients with reduced lung function in progressed LAM (60–64). Our model shows that while Rapamycin significantly suppressed the invasion of LAM-cells into the matrix it was also significantly less efficient than treatment with multi-kinase inhibitor Sorafenib. This data supports observations that multi-kinase inhibitors are able to block tumor cell growth and tumor associated angiogenesis simultaneously improving patient outcome and survival. Sorafenib is an FDA-approved multi-kinase inhibitor (37–39) that is known to inhibit RAF/MEK/ERK signalling, leading to increased tumor cell apoptosis, decreased micro-vessel density, and decreased metastatic shedding of tumor cells (37–40) and inhibit the phosphorylation of eIF4E, eukaryotic translation initiation factor, which is upregulated in LAM, downstream of mTOR (3, 39–41). Our data supports the potential for the use of multikinase inhibitors as a therapeutic option in LAM. Inclusion of LECs in the LAM organoid models only resulted in a partial inhibition of ECM invasion, suggesting that their presence antagonizes the impact of Sorafenib. In this context it is worth noting that, LECs have been shown to secrete a repertoire of growth factors, including EGF, VEGF-C, VEGF-D, which may contribute to receptor saturation of Sorafenib target receptors via the crosstalk of LAM and LEC cells. This saturation may occur through two pathways: receptor dualism and juxtacrine receptor saturation like previously described in other tumors (65). Receptor dualism refers to the

possibility that LEC-secreted chemokines and Sorafenib may compete to bind to the same receptors on the surface of LAM-cells. Alternatively, juxtacrine receptor saturation involves the presence of integrins expressed on the surface of LAM and LEC cells (66, 67), particularly α9β1-integrin on LAM organoids as previously shown (68). Given that VEGF-D can bind to both VEGFR3 and α9β1 integrin, a wedging and dual stimulation of both cell types may occur, leading to the anchoring of LECs in LAM nodules and abrogating the efficacy of Sorafenib treatment. Intergrin activation is also supported by the results of the transcriptomic data, where we have seen the integrin pathway to be highly represented in LAM nodules. Such interactions will require further investigation in our model system. While it is important to consider the potential development of resistance mechanisms, it is worth noting that the primary objective of using a multikinase inhibitor is to enhance treatment efficacy. Despite this challenge, previous studies have shown that Sorafenib and other multikinase inhibitors can effectively impede tumor progression and lower the likelihood of recurrence and metastasis. Importantly, our findings demonstrate that the observed effects of Sorafenib were superior to those of Rapamycin, indicating a more potent therapeutic effect beyond mere cytostatic activity.

Importantly, there was high concurrence between our spatialomics, kinase array data on LAM-cells, 3D pathophysiological modelling in LAM organoids and LAM tissue immunostaining in our study. From this we were able to identify TGFB1I1, also known as HIC-5, as a sorafenib sensitive gene that is known to interact with several other focal adhesion and focal adhesion-interacting proteins including VCL, PTK2, PTK2B, RHOA//B/C and HSBP1. The majority of these were upregulated in the LAM-core associated gene set. TGFB1I1 is established as a TGFβ-responsive gene that plays a role in tumor cell phenotype, cell adhesion, migration, and tissue remodeling (69). Through its role as a focal adhesion protein, and a homologue of paxillin, it is known to translocate to actin stress fibers and regulate a cells contractile capacity (70) in response to mechanical cues from changes in the extracellular environment including TGF-β signalling. Of

particular interest in LAM is the known role of HIC-5 in the induction of SMA, stimulating myofibroblast differentiation, a cellular phenotype core to LAM pathogenesis (71). Furthermore, TGFB1I1 links intracellular signaling modules to plasma membrane receptors, regulating Wnt, in addition to TGFβ signaling pathways (72, 73). Wnt signalling has been suggested as a target pathway in LAM (55, 74). The Wnt-pathway, specifically β-catenin, LATS 1 and 2 are upregulated in LAM-cells (data not shown), and are linked to loss of TSC1 and 2. Overall, our data suggests that TGFB1I1 may be important in LAM pathogenesis and highlights a need for further investigation of the cellular mechanisms driving changes associated with LAM.

Interestingly, our data also showed a significant increase in both EMP2A, laforin, a dual-specificity phosphatase) and EPHB3, a member of the Eph receptor tyrosine kinase family in response to Sorafenib. EPM2A has not been well studied in the lung though it is suggested to act as a negative regulator of mTOR signalling (75, 76). The upregulation of EPHB3 in the context of therapeutic benefit to LAM patients is less clear. Studies have identified roles in both the stimulation of (77, 78) and suppression (79, 80) of cell migration and metastasis(81) and would need to be futher studied to decipher its role in LAM pathogenesis.

In conclusion, our study has uncovered the pivotal role of LECs in facilitating LAM-cell invasion, highlighting the intricate interplay between LAM-cells and LECs in the context of Sorafenib therapy. TGFB1I1 was highlighted as a Sorafenib-regulated protein that, potentially through regulation of TGFβ and Wnt signalling established in other tissues (82, 83), may be a core regulator of differentiation and maintaining SMA expression in the LAM myofibroblast, facilitating invasion and migration and have a role in coordinating the interactions between lymphatic endothelium and metastasis of LAM-cells. Further studies will be critical to fully define the mechanisms underlying this regulation. In addition, our findings offer critical insights into LAM pathogenesis, identify Sorafenib as a potential therapeutic option, and introduce a novel 3D co-culture system that mimics LAM-nodules for studying LAM pathogenesis and evaluating potential

therapeutics. This study provides new avenues for therapeutic intervention and further research into LAM pathogenesis.

Methods:

Human lung tissue and primary cell culture: Primary human LAM cells were derived from donated explanted LAM lung as described (43, 51). De-identified lung tissue samples from patients with advanced LAM disease who had undergone lung transplantation were received from the National Disease Research Interchange (NDRI). Use of these tissues does not constitute human subjects research since all donor tissue is harvested anonymously and de-identified. LAM-cells were grown in FBM-2 media (Lonza Walkersville, Inc.) supplemented with hFGF-B (human recombinant fibroblast growth factor), Insulin, FBS (fetavl bovine serum), gentamicin as per the manufacturers instruction and maintained at 37ºC in a humidified atmosphere with 5% CO_2.

FFPE Preparation and H&E staining: H&E Staining was accomplished with assistance of the Comparative Patholofy Laboratory, Department of Pathology, University of Iowa. The slides were deparaffinized and stained in Hematoxylin and Eosin using an automated stainer.

Spheroid/Organoid culture*:*

Spheroid Formation: Spheroids were generated from primary human bronchial SMC maintained in VascuLife Media (hBrSMC, Lifeline Cell Technology, San Diego, CA) or LAM-cells. Cells were re-suspended using TrypLE (Thermo Fisher Scientific) for 5 minutes at 37°C, 5% CO_2. Cells were collected by centrifugation at 1300 rpm for 5 minutes and 500 K cells distributed into each well of an AggreWell™800 plate (24 well) (Stem Cell Technologies) as recommended by the manufacturer.

Organoid Formation: Organoids were created through the addition of primary human pulmonary lymphatic microvascular endothelial cells maintained in Endothelial Growth Medium (LECs, Angio-Proteomie, Atlanta, GA). A sequential culture approach was performed to create a LAM-nodule comprising of a core of LAM-cells cultured with LECs. On day 1 harvested SMCs and LAM-cells were resuspended in warm 15 µM CellTracker™-CMFDA (green) Working Solution and incubated for 30 min. Cells were then centrifuged and resuspended in culture media. Cells

were then seeded on AggreWell™800 plates and centrifuged to form spheroids after 24h. On day 2 LECs were lifted and labelled with CellTracker™ Red CMTPX. Labelled LECs were then seeded on the pre-formed spheroids and centrifuged at 100 x g for 3 min.

Invasion assay: For the invasion assay spheroids/organoids were embedded in growth factor reduced Matrigel. Following the formation of spheroids and organoids in AggreWell™ dishes, 600 spheroids from two AggreWell™ wells were harvested using a 2 ml serological pipette. To lift the spheroids, 1-2 ml of media was gently added to the well and collected into a 15ml falcon tube. The spheroids were then centrifuged at 280 x g for 5 minutes. Subsequently, the supernatant was removed and a mixture of 200 µl cold media and 200 µl ice-cold Geltrex was added to the spheroids/organoids to facilitate ECM embedding. An 8 µl suspension of the spheroids/organoids, aiming for approximately 12 spheroids, was then gently pipetted into each well of a 48-well dish. The dish was placed in an incubator for 10 minutes to allow the ECM to solidify before addition of 300 µl of media (with or without vehicle or drug treatments). To monitor the growth and invasion of the embedded spheroids and organoids, they were imaged daily for 72 hours using a phase contrast microscope. The images obtained were then analyzed using the image analysis tools described in the main manuscript to quantify parameters such as spheroid/organoid size, morphology and invasion into the surrounding extracellular matrix.

IF OPAL staining: Opal Multiplex Staining was used to visualize multiple proteins in a single tissue sample with same species antibodies as previously described (84, 85). Samples were either stained manually or automatically on Leica Bond RX (BOND-MAX; Leica Biosystems) following manufacturers protocols. For both methods the preparation and staining steps used the same steps. Briefly, tissue slides were prepared by deparaffinizing, dewaxing and dehydrating through ethanol incubation and rehydration with PBS washing. Epitope retrieval was performed using a microwave and AR6/AR9 buffer manually or BOND Antigen Retrieval buffer on the automated system. After blocking, primary antibodies were incubated overnight at 4°C, followed by

secondary antibody incubation at RT with HRP (RNASCOPE Multiplex Fl V2 HRP Blocker, 323107) labeled antibodies. Opal 520 or Opal 570 was incubated for 10 minutes at RT for staining. For additional antibodies the sample was treated with HRP blocker and incubated in oven at 40°C for 40 minutes and the staining steps were repeated. Finally, the samples were washed with TBST and coverslipped with a DAPI mounting medium. The antibodies used in this study are listed in **Supplemental Table S1**.

Invasion assay and image analysis: Spheroids/organoids were embedded in growth factor reduced Matrigel as described above and previously (86). To monitor the growth and invasion daily phase contrast images were collected over 72 hours. To evaluate morphology and phenotype of spheroids/organoids, an automated pipeline was developed using CellProfiler (available at https://cellprofiler.org). The pipeline was designed to enhance specific aspects of the phenotype and accurately identify both primary and secondary objects, including spheroid cores and spheroid sprouts (see **Supplemental Figure S3**). The modified pipeline allowed for a more precise quantification of various features, including size and shape, and facilitated the analysis of the spheroid/organoid behavior under different experimental conditions. Images analysis parameters: 1) **Compactness:** A filled circle will have a compactness of 1, with irregular objects or objects with holes having a value greater than 1. 2) **Perimeter:** Total length of the perimeter of the objects image. 3) **Solidity:** Equals 1 for a solid object, or <1 for an object with holes or possessing a convex/irregular boundary. 3) **Form factor:** Calculated as 4*π*Area/Perimeter2. Equals 1 for a perfectly circular object , >1 for an irregular object.

Phospho-kinase array: The phospho-kinase array and primary analysis was performed by Full moon-Biosystems (Sunnyvake, CA) following the manufacturers protocol and detailed in the Online Supplemental Methods. Briefly, after the protein concentration in the samples was measured 100 µL of DMF (Dimethylformamide) was added to 1 mg of Biotin Reagent to give a final concentration of 10 µg/µL. The samples were mixed and incubated at room temperature (RT)

for two hours in a total of 75 µl of buffer and 3 µl of Biotin/DMF mix. 35 µL of Stop Reagent was added and incubated for an additional 30 minutes at RT. For the coupling process the antibody microarray was first blocked at RT for 40 minutes, rinsed in Milli-Q water and incubated in 6mL coupling solution on an orbital shaker for 2 hours at RT. After washing, the slide was incubated Cy3-Streptavidin solution an orbital shaker for 45 minutes at RT in the dark. After another wash the slide was dried with compressed nitrogen and scanned on Axon GenePix Array Scanner.

Immunocytochemistry: Samples were fixed in PFA 0.4% (paraformaldehyde) for 15 minutes at RT or overnight at 4°C. Cells were permeabilized with Triton X 0.5% for 5 min at RT and blocked in buffer containing 5% normal donkey serum and 5% BSA for a minimum of 1 hour at RT. Incubation in primary antibody was performed for either 2 hours at RT or overnight at 4°C. Secondary antibody was applied for 2 hours at RT in the dark. Finally, 1 µg/ml DAPI solution was applied, incubated for 5 min at RT. The antibodies used for staining are induced in **Supplemental Table S1**. Spheroids were imaged in the University of Iowa Central Microscopy Research Facility (CMRF), on the Zeiss LSM710 confocal microscope and data was analyzed in Fiji 2.13.1 or using Imaris 10 (Oxford Instruments software).

Visium 10X Spatial Transcriptomic Profiling: Spatial transcriptomic profiling was performed in collaboration with the Iowa NeuroBank Core in the Iowa Neuroscience Institute (INI) and the Genomics Division in the Iowa Institute of Human Genetics (IIHG), and followed manufacturer's instructions (Doc. #CG000409, Rev. A). Briefly, two independent regions from one LAM lung donor were used to create 10 µM sections for quality control in the Comparative Pathology Laboratory (CPL) in the Department of Pathology, UIowa. Sections were H&E stained and regions of interest selected based on the presence of LAM nodules and Cysts. RNA quality was determined by extracting RNA with the Qiagen RNeasy FFPE kit (Qiagen, Hilden, Germany) and measuring RNA concentration using a Qubit fluorometer (ThermoFisher Scientific, Waltham, MA, USA) and quality determined by evaluating the samples using a 4200 Tapestation Agilent, Santa Clara, CA) in the Genomics Division of the Iowa Institute of Human Genetics. For sequencing,

10 μM FFPE sections were rehydrated, then adhered to the Visium Spatial Gene Expression Slide (PN-2000233, 10X Genomics) in a 42ºC water bath. Samples were dried in a desiccation chamber and deparaffinized using Qiagen Deparaffinization Solution for 2 hours at 60ºC. After H&E staining, brightfield tile scans of each complete section area were captured and stitched together using an Echo Revolution microscope with a 20X objective (software version 1.0.26.2). Decrosslinking was performed according to manufacturer's protocol (Doc. #CG000407, Rev. D) and immediately hybridized to the Visium Human Transcriptome Probe Kit V1.0, which contained 19,144 genes targeted by 19,902 probes. Post-probe extension, sequencing library construction was performed using unique sample indices using the Dual Index Kit TS, Set A (PN-1000251) for Illumina-compatible sequencing. Paired-end sequencing (2x100) was performed an the Novaseq 4000.

BioinformaticAnalysis of Spatial-transcriptomics: Initial data analysis was carried out in the Bioinformatics Division of the Iowa Institute of Human Genetics (IIHG). Briefly, Illumina BCL data was demultiplexed and converted to FASTQ format with Illumina's BCL2Fastq (v2.20) on IIHG servers. The resulting FASTQ sequencing data was then processed using the SpaceRanger "count" pipeline, v2.0.1, (10X Genomics) on the University of Iowa's Argon high-performance computing cluster. SpaceRanger was run with 32 local cores and 128GB of RAM on a single 56-core standard-memory node. SpaceRanger "count" carries out read alignment against the GRCh38 reference genome and the probe set which was specified as "Visium_Human_Transcriptome_Probe_Set_v1.0_GRCh38-2020-A.csv" (available as a download from 10X Genomics) and generates "feature-spot" matrices for downstream analysis. The pipeline also performs automatic tissue detection and fiducial alignment from the images." Data was evaluated and analysis performed using Loupe Browser v6.1 from .cloupe files created by the SpaceRanger pipeline, v2.0.

Ingunity pathway analysis (IPA): Analysis of the LAM-core spatialomics expression cluster completed using IPA (QIAGEN Inc., https://www.qiagenbioinformatics.com/products/ingenuity-pathway-analysis). Data with ≥1.5 Log_2-fold change was filtered to perform core analysis using "expression analysis" criteria. The gene population for calculating the p-value was limited only to the Qiagen Ingenuity Knowledge Base, with both bi-directional relationships among genes impacting interaction networks and upstream regulators. For casual network analysis to identifiy master regulators related to any disease, functions genes or chemical selections, "Kinase" was chosen only for comparison with the Full moon Kinase Assay dataset.

A list of significantly DEG from all the clusters was exported from Loupe Browser and curated (with Log2 fold change ≥ 1.5) for mapping to LungMAP. The average expression values of top 100 significant genes in the LAM-core were plotted across all other clusters as heatmap. The gene list was further refined to plot a heatmap against the Fullmoon kinase assay data using elucidean clustering method. Heatmaps were prepared using the pheatmap R-package (87) in RStudio (RStudio Team, 2020; R Core Team, 2021). LAM-core significant DEG were also mapped for their distribution across the sorted cell types in the Lung Gene Expression Analysis (LEGA) Web portal (88, 89). Code and processed data used for spatial mapping and Heatmap is available in the Git-Hub repository (https://github.com/gautam-lk/RyanLab_LAM). The cellranger matrix output file was used to predict cell type with azimuth application (90) using Human Lung Single cell dataset. LAM specific marker genes were used as query features to identify the LAM cluster cell type. A reference cell list was generated based on Azimuth cell type prediction for mapping of features and generating cell specific spatial image.

String Analysis: STRING V11.5 was used to determine protein-protein interactions with TGFB1ı1 that are functionally enriched as determined through curated databases and experimentally determined. Predicted functional partners are shown with a greater than 0.9 confidence score only.

Statistical Analysis: All data is presented as mean ± S.E.M. Statistical analysis was performed using the unpaired Student's *t* test with a value of $p<0.05$ being considered statistically significant. Unless otherwise stated the data was collected from a minimum of 3 independent experimental replicates.

Study Approval:. Lymphangioleiomyomatosis (LAM) lung samples were obtained from living donors at the time of lung transplantation through the National Disease Research Institute (NDRI, Philadelphia Pennsylvania) protocol number RKRV1. Informed consent was obtained by NDRI prior to acceptance of tissue donation for research. Identifying information were removed prior to use in accordance with institutional and NIH protocols (43, 51).

Data Availability: The data spatial-transcriptomics datasets have been deposited at GEO and are publicly available upon publication. Accession numbers are #XXX and #XXX. This paper includes original coding which is available in the Git-Hub repository (https://github.com/gautam-lk/RyanLab_LAM). Any additional information required to reanalyze the data reported in this paper is available from the lead contact upon request.

Author contributions: Designing research studies (SKG, VPK, ALR), conducting experiments (SKG, BAC, SM, NH, ALR), acquiring data (SKG, BAC), analyzing data (SKG, BAC, SM, LKG, JCN, ALR), providing reagents (BZ, ALR), writing and reviewing the manuscript (SKG, BAC, LKG, JCN, BZ, VPK, ALR), final approval of the manuscript (SKG, ALR).

Acknowledgements

Sources of support: This study was supported by The Hastings Foundation (ALR), the LAM Foundation (ALR, LAM0154SG01-22-891077), the German Research Foundation (SKG, KO5803/2-1), NIH/NHLBI (VPK, RO1 HL141462, RO1 HL158737, RO1151647, and U01HL131022).

Other acknowledgements: Mariah Leidinger, Pathology, University of Iowa prepared the tissue samples for spatial-transcriptomic processing. Visium data presented herein were obtained at the Iowa NeuroBank Core in the Iowa Neuroscience Institute (INI) and the Genomics Division in the Iowa Institute of Human Genetics (IIHG). Initial data processing and analysis was carried out by the Bioinformatics Division in the IIHG. INI is supported by the Roy J. Carver Charitable Trust and the University of Iowa Carver College of Medicine. IIHG is supported, in part, by the University of Iowa Carver College of Medicine. Opal Staining was performed in collaboration with the Translational Pathology Core Laboratory in the Department of Pathology and Laboratory Medicine at the UCLA David Geffen School of Medicine. The authors would like to acknowledge use of the University of Iowa Central Microscopy Research Facility (CMRF), a core resource supported by the University of Iowa Vice President for Research, and the Carver College of Medicine. The use of the Zeiss LSM710 confocal microscope was supported by a Shared Instrumentation grant from the NIH under award number 1 S10 RR025439-01.

References

1. Johnson S. Rare diseases. 1. Lymphangioleiomyomatosis: clinical features, management and basic mechanisms. *Thorax* 1999;54(3):254–264.

2. Kitaichi M, Nishimura K, Itoh H, Izumi T. Pulmonary lymphangioleiomyomatosis: a report of 46 patients including a clinicopathologic study of prognostic factors. *Am J Respir Crit Care Med* 1995;151(2 Pt 1):527–533.

3. Harari S, Torre O, Moss J. Lymphangioleiomyomatosis: what do we know and what are we looking for?. *European Respiratory Review* 2011;20(119):034–044.

4. Kim J, Koo B-K, Knoblich JA. Human organoids: model systems for human biology and medicine. *Nat Rev Mol Cell Biol* 2020;21(10):571–584.

5. Kwiatkowski DJ. Tuberous sclerosis: from tubers to mTOR. *Ann Hum Genet* 2003;67(Pt 1):87–96.

6. Henske EP et al. Allelic loss is frequent in tuberous sclerosis kidney lesions but rare in brain lesions. *Am J Hum Genet* 1996;59(2):400–406.

7. Cheadle JP, Reeve MP, Sampson JR, Kwiatkowski DJ. Molecular genetic advances in tuberous sclerosis. *Hum Genet* 2000;107(2):97–114.

8. Delaney SP, Julian LM, Stanford WL. The neural crest lineage as a driver of disease heterogeneity in Tuberous Sclerosis Complex and Lymphangioleiomyomatosis. *Front Cell Dev Biol* 2014;2:69.

9. Krymskaya VP, McCormack FX. Lymphangioleiomyomatosis: A Monogenic Model of Malignancy. *Annu Rev Med* 2017;68(1):69–83.

10. Henske EP, McCormack FX. Lymphangioleiomyomatosis — a wolf in sheep's clothing. *Journal of Clinical Investigation* 2012;122(11):3807–3816.

11. Henske EP, Jóźwiak S, Kingswood JC, Sampson JR, Thiele EA. Tuberous sclerosis complex. *Nat Rev Dis Primers* 2016;2(1):16035.

12. Cohen MM, Pollock-BarZiv S, Johnson SR. Emerging clinical picture of lymphangioleiomyomatosis. *Thorax* 2005;60(10):875–879.

13. Miller S et al. Evolution of lung pathology in lymphangioleiomyomatosis: associations with disease course and treatment response. *J Pathol Clin Res* 2020;6(3):215–226.

14. Black JL et al. In vitro studies of lymphangioleiomyomatosis. *Eur Respir J* 2005;26(4):569–576.

15. Hoon V, Thung SN, Kaneko M, Unger PD. HMB-45 reactivity in renal angiomyolipoma and lymphangioleiomyomatosis. *Arch Pathol Lab Med* 1994;118(7):732–734.

16. Seyama K, Kumasaka T, Kurihara M, Mitani K, Sato T. Lymphangioleiomyomatosis: a disease involving the lymphatic system. *Lymphat Res Biol* 2010;8(1):21–31.

17. Kumasaka T et al. Lymphangiogenesis in lymphangioleiomyomatosis: its implication in the progression of lymphangioleiomyomatosis. *Am J Surg Pathol* 2004;28(8):1007–1016.

18. Kumasaka T et al. Lymphangiogenesis-mediated shedding of LAM cell clusters as a mechanism for dissemination in lymphangioleiomyomatosis. *Am J Surg Pathol* 2005;29(10):1356–1366.

19. Hayashi T et al. Bronchial involvement in advanced stage lymphangioleiomyomatosis: histopathologic and molecular analyses. *Hum Pathol* 2016;50:34–42.

20. Glasgow CG, El-Chemaly S, Moss J. Lymphatics in lymphangioleiomyomatosis and idiopathic pulmonary fibrosis. *Eur Respir Rev* 2012;21(125):196–206.

21. Glasgow CG et al. Involvement of lymphatics in lymphangioleiomyomatosis. *Lymphat Res Biol* 2009;7(4):221–228.

22. Davis JM et al. Lymphatic Endothelial Differentiation in Pulmonary Lymphangioleiomyomatosis Cells. *Journal of Histochemistry & Cytochemistry* 2013;61(8):580–590.

23. Steagall WK, Zhang L, Cai X, Pacheco-Rodriguez G, Moss J. Genetic heterogeneity of circulating cells from patients with lymphangioleiomyomatosis with and without lung transplantation. *Am J Respir Crit Care Med* 2015;191(7):854–856.

24. Gupta N et al. Lymphangioleiomyomatosis Diagnosis and Management: High-Resolution Chest Computed Tomography, Transbronchial Lung Biopsy, and Pleural Disease Management. An Official American Thoracic Society/Japanese Respiratory Society Clinical Practice Guideline. *Am J Respir Crit Care Med* 2017;196(10):1337–1348.

25. Sarbassov DD et al. Prolonged rapamycin treatment inhibits mTORC2 assembly and Akt/PKB. *Mol Cell* 2006;22(2):159–168.

26. Gu X et al. Integration of mTOR and estrogen-ERK2 signaling in lymphangioleiomyomatosis pathogenesis. *Proc Natl Acad Sci U S A* 2013;110(37):14960–14965.

27. Yu J, Henske EP. mTOR activation, lymphangiogenesis, and estrogen-mediated cell survival: the “perfect storm” of pro-metastatic factors in LAM pathogenesis. *Lymphat Res Biol* 2010;8(1):43–49.

28. McCormack FX et al. Efficacy and safety of sirolimus in lymphangioleiomyomatosis. *N Engl J Med* 2011;364(17):1595–1606.

29. Cai X et al. Sirolimus decreases circulating lymphangioleiomyomatosis cells in patients with lymphangioleiomyomatosis. *Chest* 2014;145(1):108–112.

30. Folpe AL, Kwiatkowski DJ. Perivascular epithelioid cell neoplasms: pathology and pathogenesis. *Hum Pathol* 2010;41(1):1–15.

31. Sobiborowicz A et al. Feasibility and Long-Term Efficacy of PEComa Treatment—20 Years of Experience. *J Clin Med* 2021;10(10):2200.

32. Yu JJ et al. Estrogen promotes the survival and pulmonary metastasis of tuberin-null cells. *Proc Natl Acad Sci U S A* 2009;106(8):2635–2640.

33. Freise J, Klingenberg M-S, Fuge J, Welte T. Vascular endothelial growth factor (VEGF) is a predictable marker for FEV1 progression in patients with Lymphangiolyomyomatosis (LAM). In: *Rare ILD/DPLD*. European Respiratory Society; 2019:PA3685

34. Watz H et al. Lymphangioleiomyomatosis--presence of receptor tyrosine kinases and the angiogenesis factor VEGF-A as potential therapeutic targets. *Thorax* 2007;62(6):559–559.

35. Atochina-Vasserman EN et al. Pharmacological targeting of VEGFR signaling with axitinib inhibits *Tsc2* -null lesion growth in the mouse model of lymphangioleiomyomatosis. *American Journal of Physiology-Lung Cellular and Molecular Physiology* 2015;309(12):L1447–L1454.

36. Xu K-F et al. The role of vascular endothelial growth factor-D in diagnosis of lymphangioleiomyomatosis (LAM). *Respir Med* 2013;107(2):263–268.

37. Wilhelm S et al. Discovery and development of sorafenib: a multikinase inhibitor for treating cancer. *Nat Rev Drug Discov* 2006;5(10):835–844.

38. Wilhelm SM et al. Preclinical overview of sorafenib, a multikinase inhibitor that targets both Raf and VEGF and PDGF receptor tyrosine kinase signaling. *Mol Cancer Ther* 2008;7(10):3129–3140.

39. Liu L et al. Sorafenib Blocks the RAF/MEK/ERK Pathway, Inhibits Tumor Angiogenesis, and Induces Tumor Cell Apoptosis in Hepatocellular Carcinoma Model PLC/PRF/5. *Cancer Res* 2006;66(24):11851–11858.

40. Fang C et al. eIF4E-eIF4G complex inhibition synergistically enhances the effect of sorafenib in hepatocellular carcinoma. *Anticancer Drugs* 2021;32(8):822–828.

41. Evans JF et al. Inhibition of Growth of TSC2-Null Cells by a PI3K/mTOR Inhibitor but Not by a Selective MNK1/2 Inhibitor. *Biomolecules* 2019;10(1):28.

42. Grzegorek I et al. Immunohistochemical evaluation of pulmonary lymphangioleiomyomatosis. *Anticancer Res* 2015;35(6):3353–3360.

43. Goncharova EA et al. Abnormal Growth of Smooth Muscle–Like Cells in Lymphangioleiomyomatosis. *Am J Respir Cell Mol Biol* 2006;34(5):561–572.

44. Travaglini KJ et al. A molecular cell atlas of the human lung from single-cell RNA sequencing. *Nature* 2020;587(7835):619–625.

45. Guo M et al. Single-Cell Transcriptomic Analysis Identifies a Unique Pulmonary Lymphangioleiomyomatosis Cell. *Am J Respir Crit Care Med* 2020;202(10):1373–1387.

46. Zepp JA et al. Genomic, epigenomic, and biophysical cues controlling the emergence of the lung alveolus. *Science (1979)* 2021;371(6534). doi:10.1126/science.abc3172

47. Gu X et al. Integration of mTOR and estrogen–ERK2 signaling in lymphangioleiomyomatosis pathogenesis. *Proceedings of the National Academy of Sciences* 2013;110(37):14960–14965.

48. Kumasaka T et al. Lymphangiogenesis in Lymphangioleiomyomatosis. *American Journal of Surgical Pathology* 2004;28(8):1007–1016.

49. Nguyen-Vu P-A et al. Loss of tuberin, the tuberous-sclerosis-complex-2 gene product is associated with angiogenesis. *J Cutan Pathol* 2001;28(9):470–475.

50. Arbiser JL et al. Tuberous sclerosis-associated lesions of the kidney, brain, and skin are angiogenic neoplasms. *J Am Acad Dermatol* 2002;46(3):376–380.

51. Goncharova EA et al. Tuberin regulates p70 S6 kinase activation and ribosomal protein S6 phosphorylation. A role for the TSC2 tumor suppressor gene in pulmonary lymphangioleiomyomatosis (LAM). *J Biol Chem* 2002;277(34):30958–30967.

52. Robb VA, Astrinidis A, Henske EP. Frequent [corrected] hyperphosphorylation of ribosomal protein S6 [corrected] in lymphangioleiomyomatosis-associated angiomyolipomas. *Mod Pathol* 2006;19(6):839–846.

53. Clements D, Dongre A, Krymskaya VP, Johnson SR. Wild Type Mesenchymal Cells Contribute to the Lung Pathology of Lymphangioleiomyomatosis. *PLoS One* 2015;10(5):e0126025.

54. Steagall WK et al. The Lymphangioleiomyomatosis Lung Cell and Its Human Cell Models. *Am J Respir Cell Mol Biol* 2018;58(6):678–683.

55. Obraztsova K et al. mTORC1 activation in lung mesenchyme drives sex- and age-dependent pulmonary structure and function decline. *Nat Commun* 2020;11(1):5640.

56. MacDonald TJ et al. Expression profiling of medulloblastoma: PDGFRA and the RAS/MAPK pathway as therapeutic targets for metastatic disease. *Nat Genet* 2001;29(2):143–152.

57. Shah S, Sizemore GM. Diverse roles of tumor-stromal PDGFB-to-PDGFRβ signaling in breast cancer growth and metastasis. In: 2022:93–140

58. Gupta N et al. Analysis of the MILES cohort reveals determinants of disease progression and treatment response in lymphangioleiomyomatosis. *European Respiratory Journal* 2019;53(4):1802066.

59. McCormack FX et al. Efficacy and Safety of Sirolimus in Lymphangioleiomyomatosis. *New England Journal of Medicine* 2011;364(17):1595–1606.

60. Thoreen CC, Sabatini DM. Rapamycin inhibits mTORC1, but not completely. *Autophagy* 2009;5(5):725–726.

61. Bissler JJ et al. Sirolimus for Angiomyolipoma in Tuberous Sclerosis Complex or Lymphangioleiomyomatosis. *New England Journal of Medicine* 2008;358(2):140–151.

62. Choo AY, Yoon S-O, Kim SG, Roux PP, Blenis J. Rapamycin differentially inhibits S6Ks and 4E-BP1 to mediate cell-type-specific repression of mRNA translation. *Proceedings of the National Academy of Sciences* 2008;105(45):17414–17419.

63. Johnson SR et al. European Respiratory Society guidelines for the diagnosis and management of lymphangioleiomyomatosis. *European Respiratory Journal* 2010;35(1):14–26.

64. Gupta N et al. Lymphangioleiomyomatosis Diagnosis and Management: High-Resolution Chest Computed Tomography, Transbronchial Lung Biopsy, and Pleural Disease Management. An Official American Thoracic Society/Japanese Respiratory Society Clinical Practice Guideline. *Am J Respir Crit Care Med* 2017;196(10):1337–1348.

65. Majumder M et al. Co-Expression of α9β1 Integrin and VEGF-D Confers Lymphatic Metastatic Ability to a Human Breast Cancer Cell Line MDA-MB-468LN. *PLoS One* 2012;7(4):e35094.

66. Nishino K et al. Isolation and characterisation of lymphatic endothelial cells from lung tissues affected by lymphangioleiomyomatosis [Internet]. *Sci Rep* 2021;11(1):8406.

67. Black JL et al. In vitro studies of lymphangioleiomyomatosis [Internet]. *European Respiratory Journal* 2005;26(4):569–576.

68. Majumder M et al. Co-Expression of α9β1 Integrin and VEGF-D Confers Lymphatic Metastatic Ability to a Human Breast Cancer Cell Line MDA-MB-468LN. *PLoS One* 2012;7(4):e35094.

69. Gulvady AC, Dubois F, Deakin NO, Goreczny GJ, Turner CE. Hic-5 expression is a major indicator of cancer cell morphology, migration, and plasticity in three-dimensional matrices. *Mol Biol Cell* 2018;29(14):1704–1717.

70. Kim-Kaneyama J et al. Uni-axial stretching regulates intracellular localization of Hic-5 expressed in smooth-muscle cells in vivo. *J Cell Sci* 2005;118(5):937–949.

71. Varney SD et al. Hic-5 is required for myofibroblast differentiation by regulating mechanically dependent MRTF-A nuclear accumulation. *J Cell Sci* [published online ahead of print: January 1, 2016]; doi:10.1242/jcs.170589

72. Sha L, Ma D, Chen C. Exosome-mediated Hic-5 regulates proliferation and apoptosis of osteosarcoma via Wnt/β-catenin signal pathway. *Aging* 2020;12(23):23598–23608.

73. Itoh F, Watabe T. TGF-β signaling in lymphatic vascular vessel formation and maintenance. *Front Physiol* 2022;13. doi:10.3389/fphys.2022.1081376

74. Evans JF, Obraztsova K, Lin SM, Krymskaya VP. CrossTORC and WNTegration in Disease: Focus on Lymphangioleiomyomatosis. *Int J Mol Sci* 2021;22(5):2233.

75. Aguado C et al. Laforin, the most common protein mutated in Lafora disease, regulates autophagy. *Hum Mol Genet* 2010;19(14):2867–2876.

76. Kadoya M, Sasai N. Negative Regulation of mTOR Signaling Restricts Cell Proliferation in the Floor Plate. *Front Neurosci* 2019;13. doi:10.3389/fnins.2019.01022

77. Ji X-D et al. EphB3 Is Overexpressed in Non–Small-Cell Lung Cancer and Promotes Tumor Metastasis by Enhancing Cell Survival and Migration. *Cancer Res* 2011;71(3):1156–1166.

78. Li J-J et al. EphB3 Stimulates Cell Migration and Metastasis in a Kinase-dependent Manner through Vav2-Rho GTPase Axis in Papillary Thyroid Cancer. *Journal of Biological Chemistry* 2017;292(3):1112–1121.

79. Jang B et al. Expression Profile and Prognostic Significance of EPHB3 in Colorectal Cancer. *Biomolecules* 2020;10(4):602.

80. Li G et al. EphB3 suppresses non-small-cell lung cancer metastasis via a PP2A/RACK1/Akt signalling complex. *Nat Commun* 2012;3(1):667.

81. Ji X-D et al. EphB3 Is Overexpressed in Non–Small-Cell Lung Cancer and Promotes Tumor Metastasis by Enhancing Cell Survival and Migration. *Cancer Res* 2011;71(3):1156–1166.

82. Sha L, Ma D, Chen C. Exosome-mediated Hic-5 regulates proliferation and apoptosis of osteosarcoma via Wnt/β-catenin signal pathway. *Aging* 2020;12(23):23598–23608.

83. Itoh F, Watabe T. TGF-β signaling in lymphatic vascular vessel formation and maintenance. *Front Physiol* 2022;13. doi:10.3389/fphys.2022.1081376

84. Tóth ZE, Mezey É. Simultaneous Visualization of Multiple Antigens with Tyramide Signal Amplification using Antibodies from the same Species. *Journal of Histochemistry & Cytochemistry* 2007;55(6):545–554.

85. Willemsen M, Krebbers G, Bekkenk MW, Teunissen MBM, Luiten RM. Improvement of Opal Multiplex Immunofluorescence Workflow for Human Tissue Sections. *Journal of Histochemistry & Cytochemistry* 2021;69(5):339–346.

86. Sun X et al. In utero and postnatal VX-770 administration rescues multiorgan disease in a ferret model of cystic fibrosis. *Sci Transl Med* 2019;11(485). doi:10.1126/scitranslmed.aau7531

87. Kolde R. Pheatmap: pretty heatmaps. *R package version* 2012;1(2):726.

88. Du Y et al. Lung Gene Expression Analysis (LGEA): an integrative web portal for comprehensive gene expression data analysis in lung development. *Thorax* 2017;72(5):481–484.

89. Du Y, Guo M, Whitsett JA, Xu Y. 'LungGENS': a web-based tool for mapping single-cell gene expression in the developing lung: Figure 1. *Thorax* 2015;70(11):1092–1094.

90. Hao Y et al. Integrated analysis of multimodal single-cell data. *Cell* 2021;184(13):3573-3587.e29.

Figure Legends

Figure 1: Identification of LAM nodules in patient LAM lung tissue. Tiled 20x images of H&E staining of LAM lung tissue where a region of LAM nodules is highlighted at 5xZoom (yellow box). The LAM nodules are indicated with the yellow arrows and cycts with the red arrows (A). Representative images of LAM lung tissues stained with VEGFR3 (green), PDPN (yellow), HMB-45 (cyan) and SMA (red). DAPI are counterstained in all images (blue). Images are taken at 1.25x (B), 10x (C) and 20x (D). White arrows in B indicate alveolar cysts, yellow arrows in C highlight LAM nodules forming near cysts and orange arrows in D indicate PDPN and VEGFR3 expressing LEC recruited to LAM nodules. Scale bars represent 100 µm in B and C and 50 µm in D.

Figure 2: Spatial-omic analysis of LAM tissue highlights LAM-core regions. (A) H&E staining of the LAM lung region analyzed (left panel, the right panel highlights the LAM-core (blues arrows) cell cluster (purple) and the mesenchymal cells surrounding the LAM-core (green). B) t-SNE plots of the cells sequenced where the colors represent the distinct cellular clusters categorized by gene expression on one of spot transcriptome. (C) Heat map for gene expression where each column represents the color coded cell cluster. (D) Spatial localization of well established LAM genes ACTA2, VEGFD and ESR1 showing LAM nodule localization correlating to high gene expression. (E) Pie chart of selective expressed genes in the LAM-core mapped to the LungGENS human adult lung. (F) IPA pathway analysis highlighting the pathways most represented in the LAM-core gene cluster. (G) IPA predicted changes in VEGF pathway signalling based on gene expression in the LAM-core. (H) Protein expression (expressed as fold change normalized to the average signal intensity) comparing pooled protein from 3 independent LAM spheroid cultures. (I) Heat map of protein expression for proteins evaluated in the Kinase array (column 1) compared to gene expression from the spatialomics per cluster (LAM-core = purple). Green shading highlights proteins and genes highly expressed in the kinase array and LAM-core cluster.

Figure 3: Spatial-omic analysis mapped to the human lung cell atlas highlights a developmental myofibroblast phenotype associated with the LAM-core regions. (A) UMAP of the spatialomics cell clusters mapped to the human lung cell atlas with cell type identification. (B) Violin plots for established LAM-assocated genes represented across each cell cluster for as indicated on the x axis. (C) Spatial mapping of the cellular identities identified through cellular phenotyping with the lung cell atlas, SCMF and AF2 are specifically associated in regions of LAM nodules.

Figure 4: 3D spheroid models highlight increased invasion by LAM-cells. (A) Representative images of spheroid formation in aggrewell plates at the day of seeding and 24 hrs later. The inset images highlight the formation of spheroids by 24 hrs. (B) Representative phase images of the spheroids at Day 1 and quantification of spheroid size shown as area in pixels per unit from measurement of spheroids generated in 2 independent experiments per cell type. Data represents mean±S.E.M. (C) Representative images of embedded SMC and LAM spheroid on Day 3 and Day 5 showing time dependent changes in spheroid interaction with the ECM for SMC (top) and LAM cell (bottom) spheroids. (D) 5x zoom images of spheroids showing the different phenotype of SMC and LAM spheroids. (E) Quantification of changes in the perimeter of the spheroids over 5 days comparing LAM and SMC spheroids. Each dot indicates a spheroid and a minimum of 20 (range 20-112) spheroids were measured from a minimum of 3 independent experiments. Data shown represents the mean±SEM, ****$p<0.0001$. (F) Representative image of a LAM spheroid showing SMA (Green) and PDGFRα (red) expression. (G) Representative confocal images with surface mapping of the spheroid (purple) and the density of expression of PDGFRα features in red with SMA expression (green). The scale bars in A-B, D are 920 µm, in F and G represent 20 µm.

Figure 5: LAM-LEC organoids have increased invasion into the ECM. (A) Representative images of pre-formed core spheroids of either LAM-cells or SMCs with floating LECs. Scale bar represents 930µm. (B) Celltracker green-labelled core spheroid of LAM-cells with floating Celltracker red-labelled LECs. Scale bar represents 300µm. (C) Representative IF images of LAM-LEC organoids in suspension 24h after seeding LECs on the core spheroid. SMC marked by SMA (red) and LEC marked by PDPN (green). Scale bars represent 250 µm. (D) Representative images of SMC-LEC (top) and LAM-LEC (bottom) organoids embedded in ECM. The 5xzoom images focus on sprouting, invading the ECM from the spheroid core. (E) Cell profiler analysis of organoid invasion highlighting Solidarity, Compactness and Perimeter comparing control SMC-LEC organoids to LAM-LEC organoids. (F-G) Representative confocal IF image of LAM-LEC organoids with LAM-cell (green) and LECs (red) in suspension and embedded, showing sprouting into the matrix evident. In all experiments N=9 experimental repeats, Data shown represents mean±SEM, ****$p<0.0001$.

Figure 6: Sorafenib treatment inhibits migration and invasion of LAM spheroids and LAM-LEC organoids. Representative phase contrast images of LAM-spheroids grown in vehicle (A) or the presence of 7 µM Sorafenib (B). (C) Changes in solidity, perimeter and comparing Sorafenib treated spheroids to vehicle. Representative phase contrast images of LAM-LEC organoids grown in vehicle (D) or the presence of 7 µM Sorafenib (E). (F) Changes in solidity, perimeter and comparing Sorafenib treated spheroids to vehicle. In all experiments N=9 experimental repeats, Data shown represents mean±SEM, ****$p<0.0001$, **$p<0.01$. Scale bars represent 930 µm. Data representing the perimeter (G) and Form Factor (H) comparing vehicle treated controls to rapamycin treated (20 µM) and Sorafenib treated (7 µM) LAM-spheroids. (I) Representative images (5xZoom) of spheroids from each of these conditions.

Figure 7: TGFB1ı1 is a Sorafenib targeted kinase that is significantly reduced in the LAM-nodule models. (A) Fold change of proteins targeted by 7µm Sorafenib in LAM spheroids. A significant fold change is considered, when the value is less then 0.5 or greater than 2.0, indicating that the protein amount either decreased by 50% (0.5) or doubled (2.0). Blue indicates increased expression levels and red indicates decreased expression after Sorafenib treatment. (B) STRING analysis of functional protein interactions of TGFB1ı1 related to β-catenin binding determined through GO pathways (red, top panel) and VEGF signaling, determined through reactome and KEGG pathways (red and blue, bottom panel) with greater than 0.9 confidence score. (C) Spatialomics maps of gene expression distribution and violin plots for gene expression per identified lung cell atlas cluster for TGFB1ı1 and associated proteins HSBP1 and VCL. The yellow highlights the predominant LAM-core associated cell type.

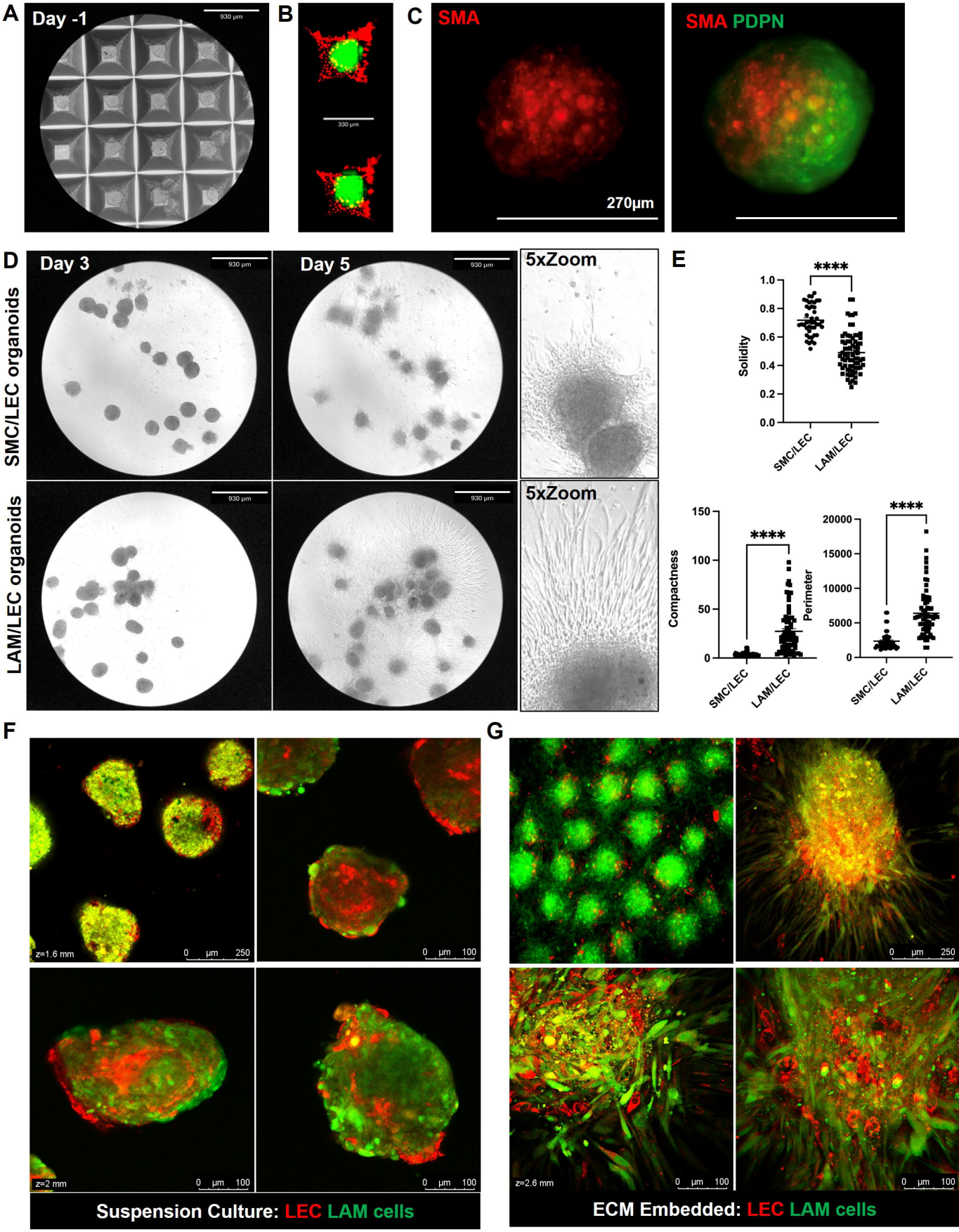
A
Day -1
930 µm
B
330 µm
C
SMA
270µm
SMA PDPN
D
Day 3
Day 5
5xZoom
SMC/LEC organoids
LAM/LEC organoids
E
****
Solidity
SMC/LEC
LAM/LEC
Compactness
Perimeter
F
z=1.6 mm
z=2 mm
Suspension Culture: LEC LAM cells
G
z=2.6 mm
ECM Embedded: LEC LAM cells

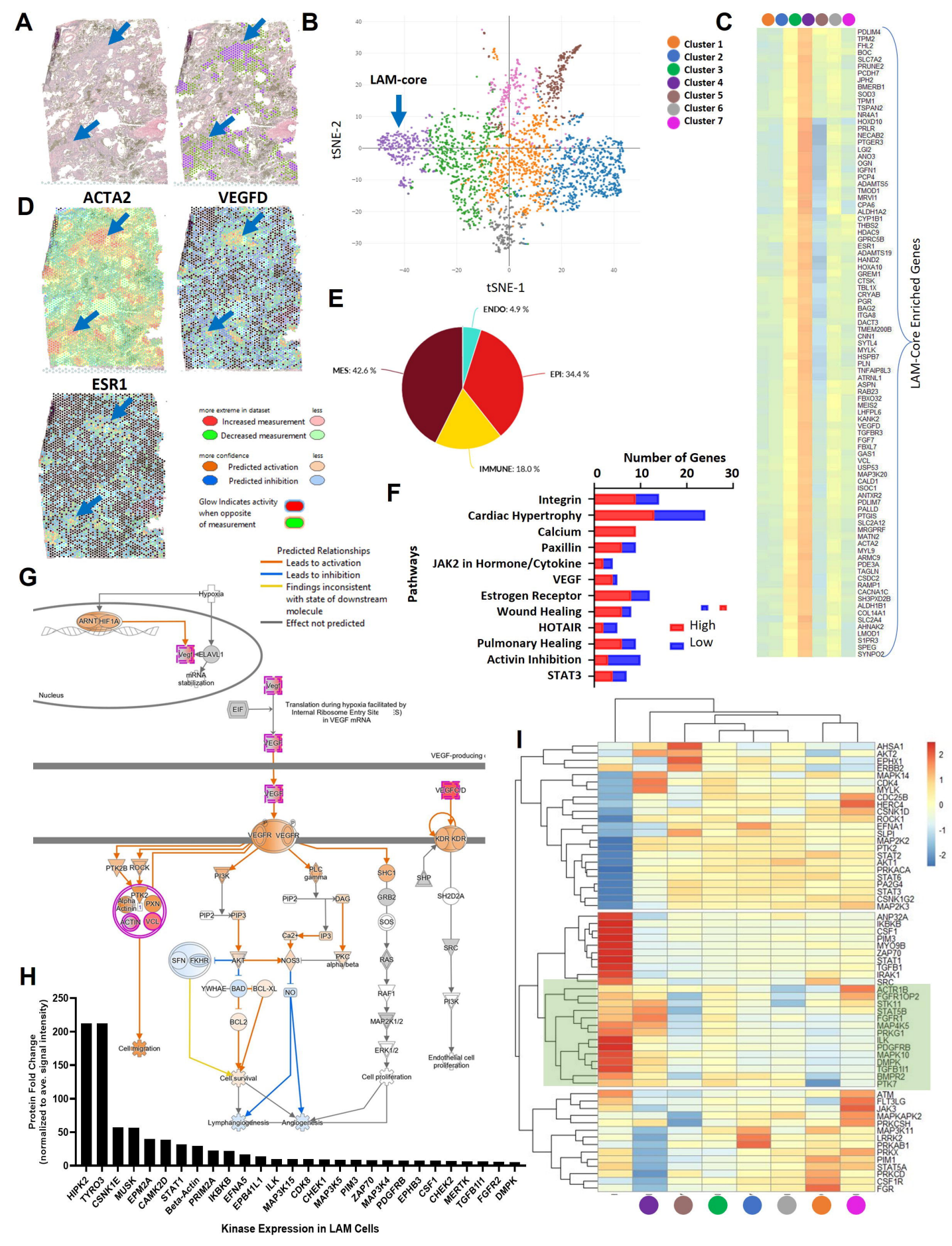
A
B
LAM-core
tSNE-2
tSNE-1
Cluster 1
Cluster 2
Cluster 3
Cluster 4
Cluster 5
Cluster 6
Cluster 7
C
LAM-Core Enriched Genes
D
ACTA2
VEGFD
ESR1
more extreme in dataset
less
Increased measurement
Decreased measurement
more confidence
Predicted activation
Predicted inhibition
Glow Indicates activity when opposite of measurement
E
ENDO: 4.9 %
EPI: 34.4 %
IMMUNE: 18.0 %
MES: 42.6 %
F
Number of Genes
Pathways
Integrin
Cardiac Hypertrophy
Calcium
Paxillin
JAK2 in Hormone/Cytokine
VEGF
Estrogen Receptor
Wound Healing
HOTAIR
Pulmonary Healing
Activin Inhibition
STAT3
High
Low
G
Predicted Relationships
Leads to activation
Leads to inhibition
Findings inconsistent with state of downstream molecule
Effect not predicted
Hypoxia
ARNT HIF1A
Vegf
ELAVL1
mRNA stabilization
Nucleus
EIF
Translation during hypoxia facilitated by Internal Ribosome Entry Site (IRES) in VEGF mRNA
VEGF
VEGF-producing
VEGFR VEGFR
KDR KDR
VEGFC/D
PTK2B ROCK
PI3K
PLC gamma
SHC1
SHP
PTK2 Alpha Actinin 1 PXN ACTIN VCL
PIP2
PIP3
DAG
GRB2
SH2D2A
Ca2+
IP3
SOS
SFN FKHR
AKT
NOS3
PKC alpha/beta
RAS
SRC
YWHAE BAD BCL-XL
NO
RAF1
PI3K
BCL2
MAP2K1/2
ERK1/2
Cell migration
Cell survival
Cell proliferation
Endothelial cell proliferation
Lymphangiogenesis
Angiogenesis
H
Protein Fold Change (normalized to ave. signal intensity)
HIPK2
TYRO3
CSNK1E
MUSK
EPM2A
CAMK2D
STAT1
Beta-Actin
PRIM2A
IKBKB
EFNA5
EPB41L1
ILK
MAP3K15
CDK8
CHEK1
MAP3K5
PIM3
ZAP70
MAP3K4
PDGFRB
EPHB3
CSF1
CHEK2
MERTK
TGFB1I1
FGFR2
DMPK
Kinase Expression in LAM Cells
I

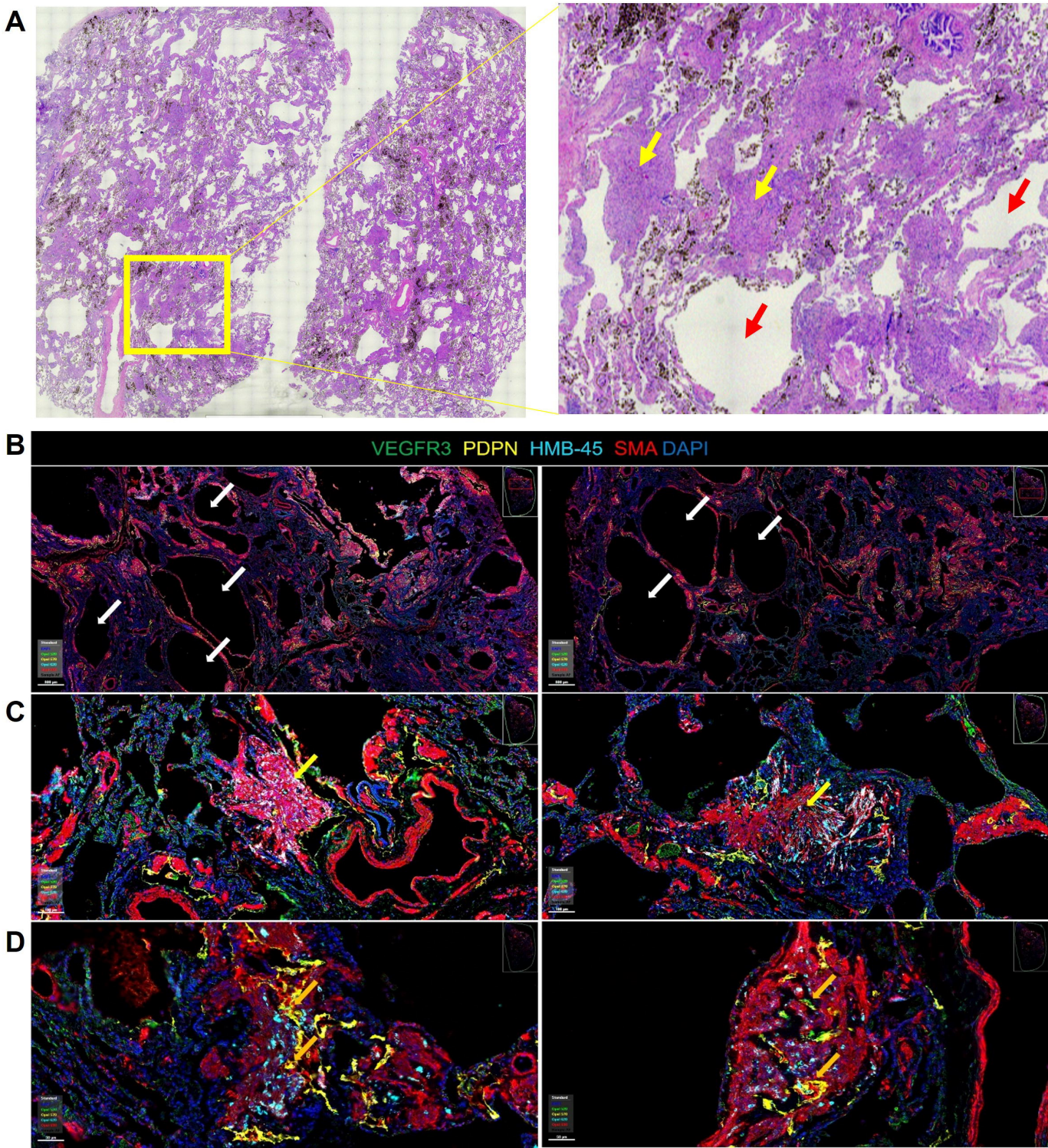
A
B
VEGFR3 PDPN HMB-45 SMA DAPI
C
D

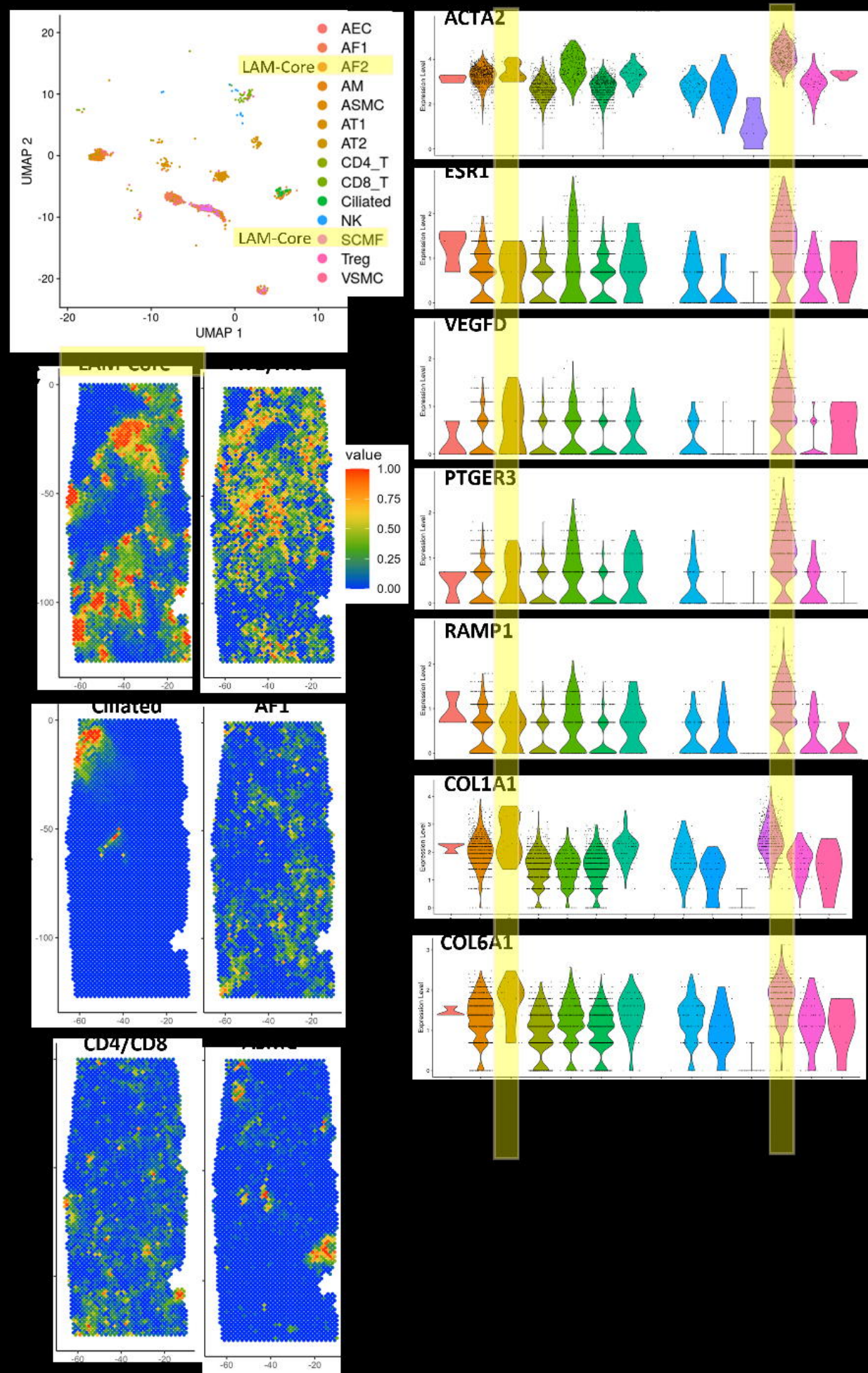
AEC
AF1
LAM-Core
AF2
AM
ASMC
AT1
AT2
CD4_T
CD8_T
Ciliated
NK
LAM-Core
SCMF
Treg
VSMC
UMAP 2
UMAP 1
value
1.00
0.75
0.50
0.25
0.00
Ciliated
AF1
CD4/CD8
ACTA2
ESR1
VEGFD
PTGER3
RAMP1
COL1A1
COL6A1
Expression Level

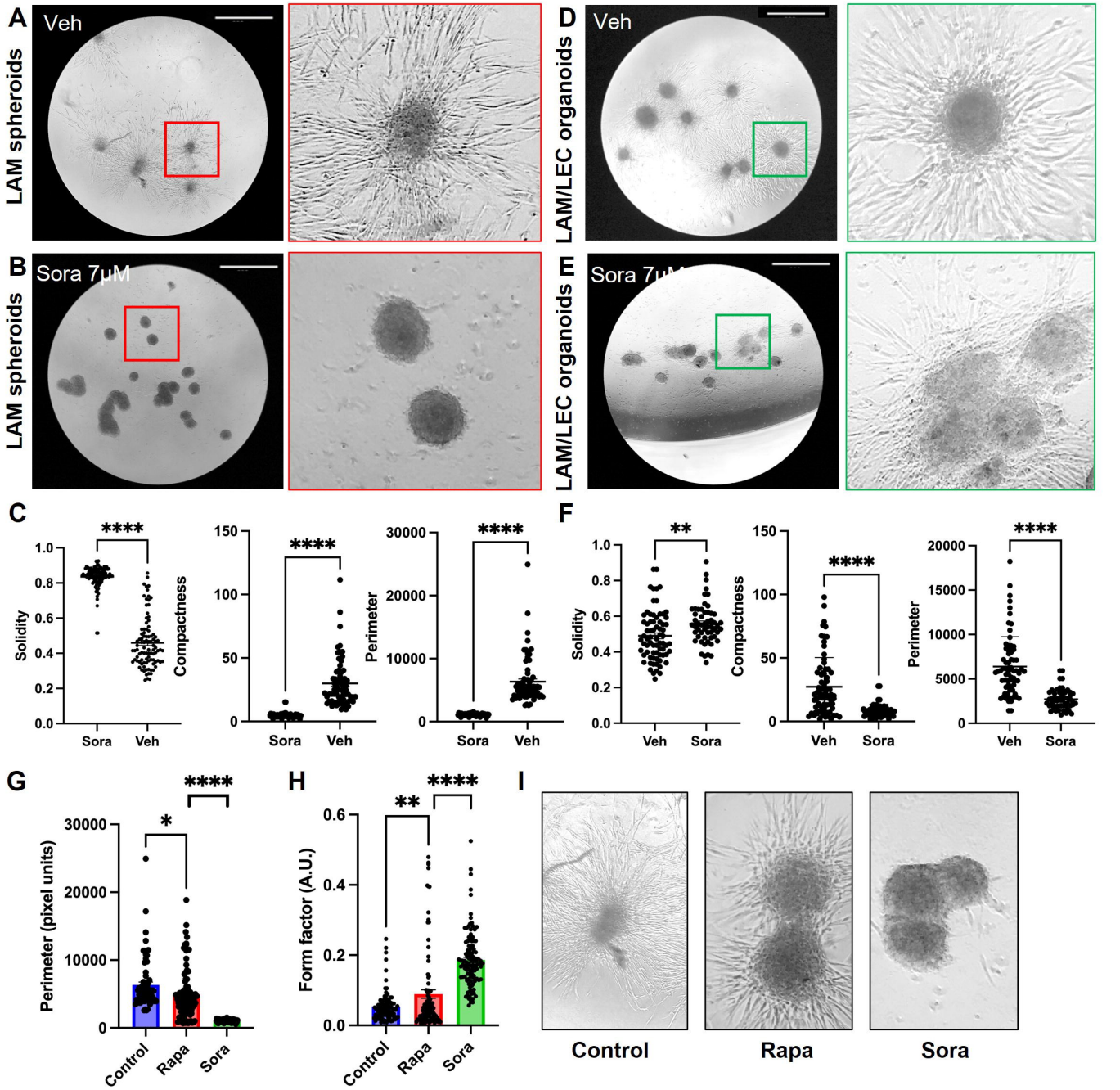
A
Veh
LAM spheroids
B
Sora 7μM
LAM spheroids
D
Veh
LAM/LEC organoids
E
Sora 7μM
LAM/LEC organoids
C
Solidity
Compactness
Perimeter
Sora
Veh
****
F
Solidity
Compactness
Perimeter
Veh
Sora
**
****
G
Perimeter (pixel units)
Control
Rapa
Sora
*
****
H
Form factor (A.U.)
Control
Rapa
Sora
**
****
I
Control
Rapa
Sora

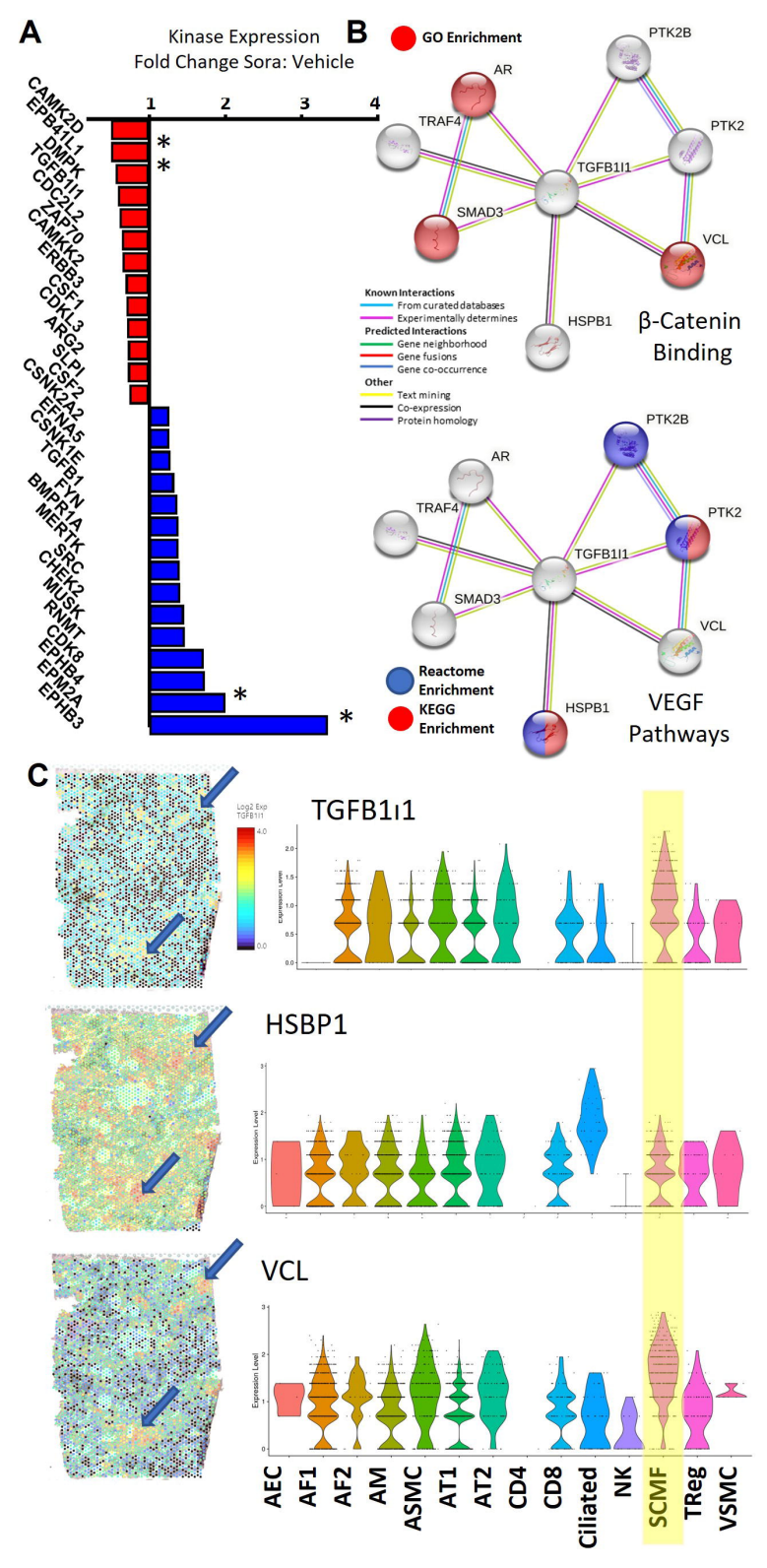
A
Kinase Expression
Fold Change Sora: Vehicle
1
2
3
4
CAMK2D
EPB41L1
DMPK
TGFB1I1
CDC42
ZAP70
CAMKK2
ERBB3
CSF1
CDK13
ARG2
SLP1
CSF2
CSNK2A2
EFNA5
CSNK1E
TGFB1
FYN
BMPR1A
MERTK
SRC
CHEK2
MUSK
RNMT
CDK8
EPHB4
EPMA
EPHB3
B
GO Enrichment
PTK2B
AR
TRAF4
PTK2
TGFB1I1
SMAD3
VCL
HSPB1
Known Interactions
From curated databases
Experimentally determines
Predicted Interactions
Gene neighborhood
Gene fusions
Gene co-occurrence
Other
Text mining
Co-expression
Protein homology
β-Catenin Binding
Reactome Enrichment
KEGG Enrichment
VEGF Pathways
C
TGFB1I1
HSBP1
VCL
Log2 Exp TGFB1I1
Expression Level
AEC
AF1
AF2
AM
ASMC
AT1
AT2
CD4
CD8
Ciliated
NK
SCMF
TReg
VSMC

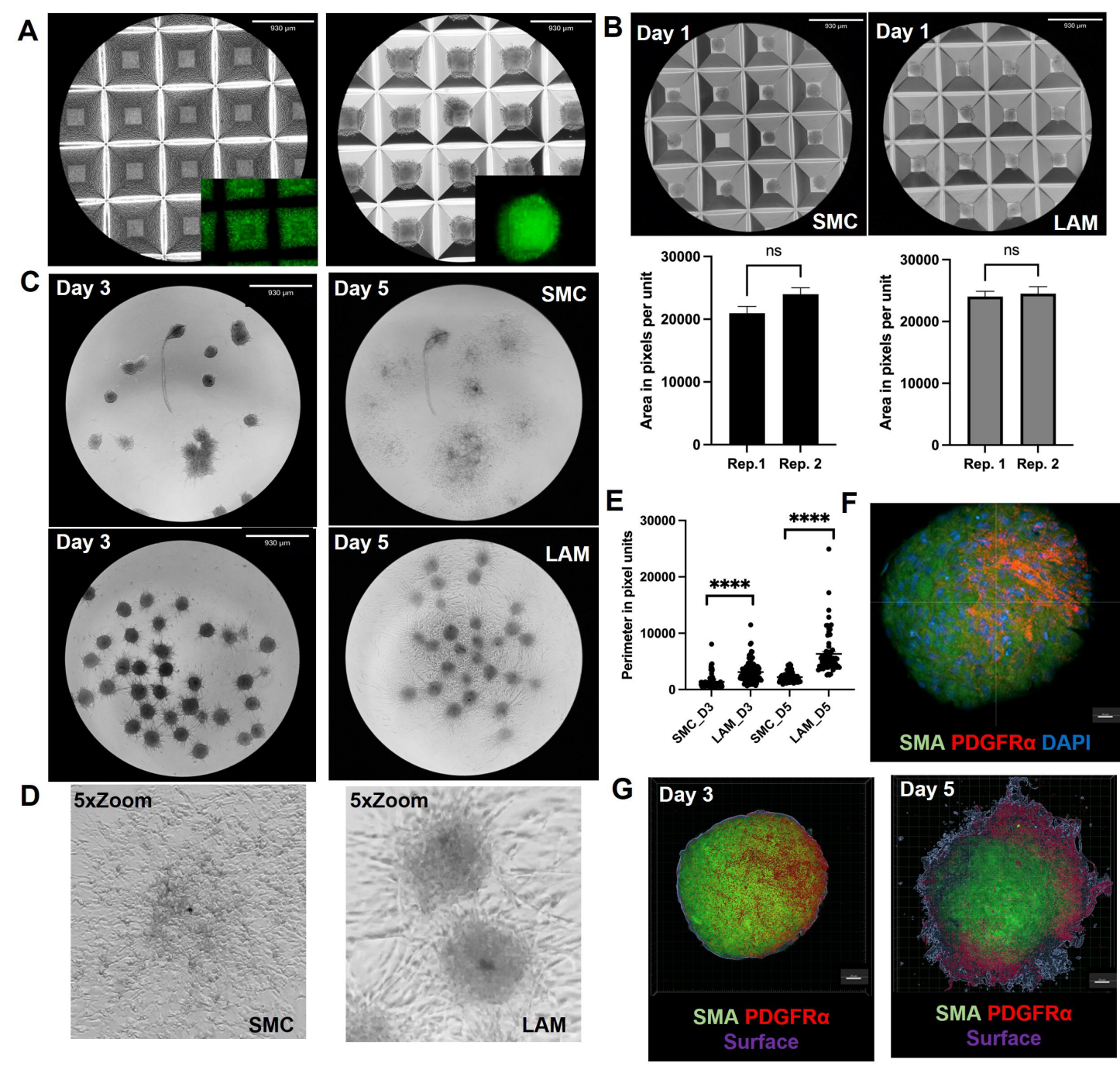
A
930 µm
930 µm
B
Day 1
930 µm
SMC
Day 1
930 µm
LAM
ns
Area in pixels per unit
30000
20000
10000
0
Rep.1
Rep. 2
ns
Area in pixels per unit
30000
20000
10000
0
Rep. 1
Rep. 2
C
Day 3
930 µm
Day 5
SMC
Day 3
930 µm
Day 5
LAM
E
Perimeter in pixel units
30000
20000
10000
0
****
****
SMC_D3
LAM_D3
SMC_D5
LAM_D5
F
SMA PDGFRα DAPI
D
5xZoom
SMC
5xZoom
LAM
G
Day 3
SMA PDGFRα
Surface
Day 5
SMA PDGFRα
Surface